Experimental Mechanics (2011) 51:1379–1393
DOI 10.1007/s11340-010-9441-4

Techniques and Applications of the Simulated Pattern Adaptation of Wilkinson's Method for Advanced Microstructure Analysis and Characterization of Plastic Deformation

C.J. Gardner · J. Kacher · J. Basinger · B.L. Adams · M.S. Oztop · J.W. Kysar

Received: 31 August 2010 / Accepted: 14 November 2010 / Published online: 8 December 2010

Abstract Electron Backscatter Diffraction (EBSD) based Orientation Imaging Microscopy (OIM) is used routinely at ~500 materials laboratories worldwide for the characterization and development of diverse crystalline materials. Statistically significant data sets (~10^7 individual EBSD measurements) can be collected and analyzed within time periods of acceptable beam stability (~10^5s). However, limitations in angular and spatial resolution have motivated a continued search for more robust EBSD-based methods. Herein is a gathered presentation of advanced techniques in use, intended as a guide to researchers in selecting the most appropriate method for their work. Wilkinson's method has been shown to increase angular resolution nearly two orders of magnitude to ±0.006°, facilitating measurement of elastic strain, lattice curvature, and dislocation density. A simulated pattern adaptation of Wilkinson's method extends these measurement capabilities to polycrystalline materials, by avoiding the need for an experimental strain free reference pattern. The angular resolution limit obtained is ~0.04°. Accurate pattern center calibration, essential to the high resolution methods, is accomplished by parallelization of band edges projected onto a sphere centered at the interaction volume. FFT powered cross-correlation functions improve the spatial resolution near grain boundaries and correct for measurement inaccuracies induced by overlapping patterns. To corroborate these claims, exemplary results taken from a wedge-indented nickel single crystal, cold-worked copper polycrystal, and rolled nickel polycrystal are shown.

Keywords Cross-correlation · EBSD · OIM · Pattern center · Simulated pattern method · Wilkinson's method

C. Gardner (✉) · J. Kacher · J. Basinger · B. Adams
Department of Mechanical Engineering,
Brigham Young University,
435 CTB,
Provo, UT 84602, USA
e-mail: CalvinJGardner@gmail.com

M. Oztop · J. Kysar (SEM member)
Columbia University,
500 W. 120th Street,
New York, NY 10027, USA

Introduction

Significant progress in materials development strongly correlates with advances in observational capabilities. One example among many that could be cited is the recent trend to examine the microstructure characteristics of fatigue crack initiation sites. The ability to characterize the local crystal phase and orientation field, occurring at an observed site of fatigue crack nucleation, opens the door to studies of the local response fields (stress and strain), and their co-location with dislocation slip activity, weak interfaces and other characteristics [1, 2]. These correlations, which are currently proving to be fruitful in the study of damage physics, would not be possible without the advances in microscopy capable of resolving lattice phase and orientation at the micron scale.

Crystallographic information is swiftly obtained by directing a stationary electron beam at a tilted sample and analyzing the resulting pattern of diffracted electrons. The diffraction pattern is characteristic of the area from which it originated; and with the advanced capabilities described in this paper, can be used to measure crystal orientation, differentiate material phase, locate grain boundaries, measure interface misorientation, map elastic strain, determine

lattice curvature, recover the geometrically necessary dislocation density, and locate minuscule cracks and imperfections in the material. If measurements of these properties are of sufficient accuracy and precision, a new world of application specific material design is open to engineers. At present, commercially available Orientation Imaging Microscopy (OIM) systems are commonly used to quickly determine crystal orientation and map grain structure. However, the angular resolution in lattice orientation of standard OIM is limited to ~0.5° and the spatial resolution to approximately 100 nm [3, 4]. While standard OIM is satisfactory for many applications, in order to obtain more complete information about material microstructure, advanced techniques must be employed.

Each grouping of diffraction patterns has associated with it an information set containing much of the potential knowledge that may be garnered from the patterns. This information is contained in the angles, widths, clarity, and intensities of the Kikuchi bands, in addition to their relative shifts and imperfections. The purpose of this paper is to outline, discuss, and provide examples of various advanced techniques used to improve angular, spatial, and strain resolution for the measurement of geometrically necessary dislocation, grain boundary location, lattice curvature, orientation, and elastic strain. Wilkinson's method, and its simulated pattern adaption in particular, will be discussed in detail.

Materials and Methods

EBSD Overview

Before delving into the particulars of diffraction pattern analysis, a basic overview of EBSD is provided. An EBSD system consists of a Scanning Electron Microscope (SEM), a sample tilted at 70° from the horizontal, and a phosphor screen with a CCD (Charge Coupled Device) camera to view the diffraction patterns. For EBSD, a beam of electrons is directed to a point of interest on a tilted crystalline sample as shown in Fig. 1. The incident electrons are diffracted from planes within the crystalline sample according to Bragg's Law. Diffracted electrons from a particular plane form a pair of wide angle cones. When these cones intersect the fluorescent phosphor screen the intense area between them is known as a Kikuchi band. The center-line of a Kikuchi band nominally corresponds to the intersection of the diffracting plane with the phosphor screen. Therefore, each band may be indexed by its Miller indices with each intersection of band-pairs labelled by the common zone axis.

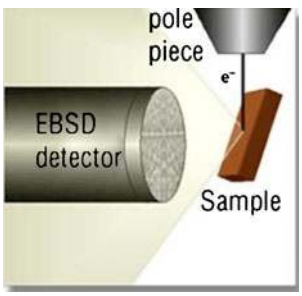

Fig. 1 Schematic of SEM. The electron beam from the pole piece diffracts off the sample and forms a pattern on the screen of the EBSD detector. Figure courtesy of TSL

Patterns are commonly indexed automatically utilizing a Hough/Radon transform to represent Kikuchi band positions. A line co-linear with the Kikuchi band becomes a point of intensity in Hough space as given by the following equation:

$$r(\theta) = x\cos\theta + y\sin\theta \tag{1}$$

where x and y correspond to a point on the line. Each point along the line produces a trigonometric function and all the functions from a particular line will intersect to form a distinct point; when multiple lines are considered an intensity spot of finite size occurs, having the characteristic butterfly shape of the trigonometric functions demonstrated in Fig. 2. The peak is located at the angle θ_0, that forms a perpendicular intersection to the Kikuchi band, and the radial distance r_0 at that angle. Therefore, the Hough transform of a measured pattern consists of numerous intensity peaks spread across Hough space with each peak corresponding to one Kikuchi band in the pattern. Knowledge of the diffraction planes in the crystal lattice is then used to index the pattern and obtain the associated crystal orientation.

The limiting factor of traditional OIM's spatial resolution is the size of the interaction volume (the sample volume that diffracts electrons to the phosphor screen), which is primarily dependent upon the electron beam accelerating voltage, material atomic number (typically, larger Z-numbers result in smaller interaction volumes), sample tilt, and probe current [5, 6]. The EBSD pattern recorded and indexed by traditional OIM is actually an average of the information contained within the interaction volume. Using known parameters the approximate interaction volume diameter can be simulated, and has been found by various authors to be in the range of 50–100 nm for heavier metals (Fe, Ni, Cu) and 100–200 nm for lighter metals (Al, Mg) [7, 8]. The concomitant spatial resolution is dependent on how precisely mixed patterns near grain boundaries can be distinguished, and is often approximated as half the interaction volume diameter [9]. Further, the angular resolution of OIM depends upon the measurement of the Kikuchi band position, and is in the range of±0.5° [3, 4]. Unfortunately, for small misorientations the angular uncer-

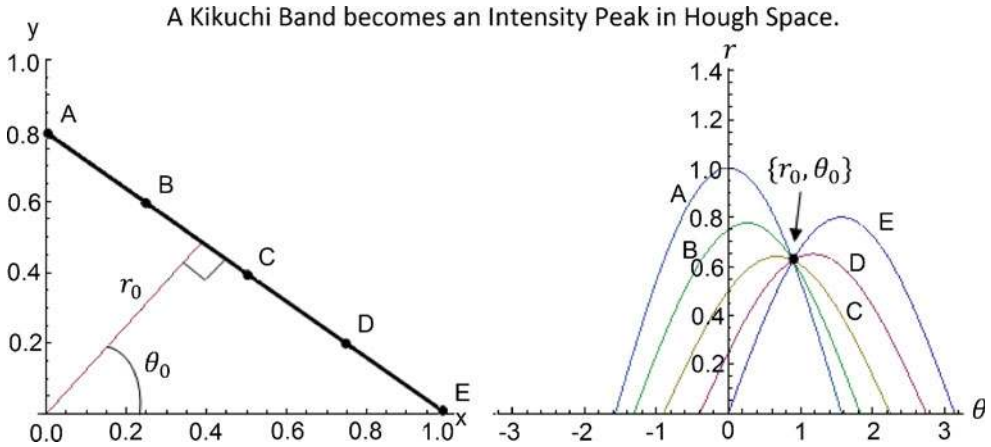

Fig. 2 The Hough Transform: A line from the EBSD pattern is converted to an intensity peak in Hough space. Points A-E on the left correspond to functions A-E on the right

tainty in individual measurements propagates into large errors in determining the misorientation axis. Bate et al. have developed an analytical relationship for the expected error [8]:

$$\phi = \arctan\left[\frac{\delta}{\varphi}\right] \tag{2}$$

where ϕ is the error in the misorientation axis, δ is the orientation measurement error, and φ is the angle of the misorientation being measured. Obviously, for small angles of misorientation even small errors in orientation measurement propagate into large errors in the misorientation axis. These errors are reduced significantly by Wilkinson's method.

Wilkinson's Method Overview

The work of Troost et al. and Wilkinson et al. has greatly improved the angular resolution of EBSD analysis [10, 11]. Their cross-correlation based method increases angular sensitivity by two orders of magnitude beyond the Hough/Radon transform. This enhanced resolution is an extremely important advance. For example, the improved resolution can separate some of the cubic coincidence site lattice (CSL) boundaries, such as ∑13b and ∑17a which differ by only 0.3°, and ∑7 and ∑9 which differ by 0.7°. Proper distinction of the minimum axis of rotation also augments the reliability of CSL determination. And the reduced error in misorientation axis determination is sufficient to enable an estimation of lattice curvature, to recover some components of Nye's dislocation tensor [12]. Moreover, increased accuracy facilitates the partial recovery of the elastic displacement gradient tensor (the entire tensor is recovered if appropriate traction-free boundary conditions are imposed).

Wilkinson's method compares two measured EBSD patterns utilizing the small shifts in position of pattern features to determine the difference in strain and orientation between the patterns. Therefore, in order to obtain absolute measurements, one of the two compared patterns must be a strain free reference pattern at (or near) the correct orientation. The patterns are compared by selecting a number of regions of interest (ROIs) distributed over each pattern. The cross-correlation between ROIs in the reference and experimental patterns are then calculated using Fourier Transforms as follows:

$$C = \Im^{-1}\{\Im\{f\}^{*}conj(\Im\{g\})\} \tag{3}$$

where $\Im\{\ \}$ is the Fourier transform, *conj*( ) is the complex f conjugate, and g are corresponding ROIs from the two patterns, * indicates the element wise multiplication of matrices, and C is the resulting image. The line emanating from the pattern center to the peak in each of the ROI cross-correlations gives the shift vector q (measured on the phosphor) for that ROI. Interpolation methods are used to obtain sub-pixel resolution. It should be noted that proper filtering of the measured EBSD pattern, to remove dark spot defects and non-uniform intensity, is required to obtain accurate shift vectors [13–15]. After filtering, the shift is assumed to be equal to the average shift in the center of the ROI and is measured perpendicular to $\hat{r}$ (the unit vector pointing from the specimen origin to the ROI center on the phosphor screen). The components of the shift at the center of each ROI are related to the components of the displacement gradient tensor D by the expression:

$$q = D\hat{r} - (D\hat{r}\cdot\hat{r})\hat{r} \tag{4}$$

with

$$D = \begin{pmatrix} \frac{\partial u_1}{\partial x_1} & \frac{\partial u_1}{\partial x_2} & \frac{\partial u_1}{\partial x_3} \\ \frac{\partial u_2}{\partial x_1} & \frac{\partial u_2}{\partial x_2} & \frac{\partial u_2}{\partial x_3} \\ \frac{\partial u_3}{\partial x_1} & \frac{\partial u_3}{\partial x_2} & \frac{\partial u_3}{\partial x_3} \end{pmatrix} \tag{5}$$

where $u=(u_1, u_2, u_3)$ is the displacement at the position $x=(x_1, x_2, x_3)$. Combining equations for components of q results in two simultaneous equations [16]:

$$r_3 q_1 - r_1 q_3 = r_1 r_3 \left(\frac{\partial u_1}{\partial x_1} - \frac{\partial u_3}{\partial x_3} \right) - r_1 r_2 \frac{\partial u_3}{\partial x_2} + r_2 r_3 \frac{\partial u_1}{\partial x_2} - r_1^2 \frac{\partial u_3}{\partial x_1} + r_3^2 \frac{\partial u_1}{\partial x_3} \tag{6a}$$

$$r_3 q_2 - r_2 q_3 = r_2 r_3 \left(\frac{\partial u_2}{\partial x_2} - \frac{\partial u_3}{\partial x_3} \right) - r_1 r_2 \frac{\partial u_3}{\partial x_1} + r_1 r_3 \frac{\partial u_2}{\partial x_1} - r_2^2 \frac{\partial u_3}{\partial x_2} + r_3^2 \frac{\partial u_2}{\partial x_3} \tag{6b}$$

The terms $\left(\frac{\partial u_1}{\partial x_1} - \frac{\partial u_3}{\partial x_3}\right)$ and $\left(\frac{\partial u_2}{\partial x_2} - \frac{\partial u_3}{\partial x_3}\right)$ each represent a single unknown for a total of eight unknowns in the two equations. Therefore, shift measurements must be made for at least 4 ROIs to obtain a solution to the simultaneous equations. Any additional ROI measurements are used in a standard matrix least squares method to determine the best-fit solution. It should be noted that experimental recovery of the full displacement gradient tensor necessarily assumes only elastic deformation to have occurred.

Unfortunately, Wilkinson's method cannot fully resolve the terms on the diagonal of D. Since a spherical dilation of the crystal lattice generates no shift in the EBSD patterns, only the differences between the diagonal terms can be determined. Though, with knowledge of the crystal elastic constants, traction-free boundary conditions may be applied, consistent with the presence of the free surface of the sample, and the final of the 9° of freedom can be resolved.

Once the displacement gradient tensor is determined it is a simple step to find the strain tensor and the rotation tensor as follows:

$$\varepsilon_{ij} = \frac{1}{2}\left(\frac{\partial u_i}{\partial x_j} + \frac{\partial u_j}{\partial x_i} \right) \tag{7a}$$

and

$$\omega_{ij} = \frac{1}{2}\left(\frac{\partial u_i}{\partial x_j} - \frac{\partial u_j}{\partial x_i} \right) \tag{7b}$$

where ε, the infinitesimal strain tensor, is the symmetric part of D, and ω, the infinitesimal rotation tensor, is the anti-symmetric part. Wilkinson concluded (and the authors have confirmed) that by using the cross-correlation method to compare patterns directly the components of the strain and rotation tensors can be determined to a resolution of $\pm 10^{-4}$ consistent with a misorientation resolution of ±0.006°. This is an improvement of nearly two orders of magnitude over the standard Hough/Radon transform method.

Wilkinson's method represents a substantial advance in the angular and strain resolution of EBSD analysis and opens the door for accurate analysis of lattice curvature, elastic strain, and geometrically necessary dislocation (GND) densities. However, without a strain free pattern the Wilkinson method is limited to measuring gradients of elastic strain and lattice orientation rather than absolute values. This makes comprehensive application of Wilkinson's method to a polycrystalline sample difficult, particularly for small grain sizes and plastically deformed samples. The simulated pattern method presented in the recent work of Kacher et al. offers a solution to these difficulties [17].

Simulated Pattern Method Overview

In order to avoid the difficulty of obtaining a strain free pattern, it is possible to use a simulated reference pattern. Because high fidelity simulations are computationally expensive [18], the simulated pattern method uses a simple kinematical model (Bragg's Law based) to generate a strain-free reference pattern. By iteratively generating these simple patterns at each calculated deformation state of a measured pattern, and then repeating the calculation with the new simulation, a high resolution result is rapidly found by convergence.

The deformation tensor F, which is related to D by the expression $F=D+I$, determines how diffraction cones are oriented with respect to the phosphor frame and may also alter the inter-planar spacing d_{hkl}. Combining the equation for a cone with the various parameters determining orientation and intensity results in the following equation for a simulated Kikuchi Band [17]:

$$B(\vec{p}, F, R^{v\to c}, R^{c\to co}, (hkl)) = \begin{cases} S_{hkl}^2 & f\left([R^{c\to co} F R^{v\to c}\vec{p}]_1\right)^2 + \left([R^{c\to co} F R^{v\to c}\vec{p}]_2\right)^2 \geq \left(\frac{\left([R^{c\to co} F R^{v\to c}\vec{p}]_3\right)}{\tan\theta}\right)^2 \\ 0 & otherwise \end{cases} \tag{8}$$

where B is the simulated band, $\vec{p}$ represents a point in the phosphor screen reference frame v, $R^{v\to c}$ is the rotation tensor from the phosphor screen frame to the crystal frame c, $R^{c\to co}$ is the rotation tensor from the crystal frame to the cone reference frame co, (hkl) is the chosen diffraction plane, θ is the cone angle, and S_{hkl} is the structure intensity factor. Summing the contributions of each band and its symmetry variants generates the complete approximation of the EBSD image, thus:

$$I(\vec{p},f) = \sum_i \sum_j B\left(\vec{p}, F, S^{(i)}, (hkl)^{(j)}\right) \tag{9}$$

where I is the composite image, $S^{(i)}$ are the elements of the symmetry subgroup, and $(hkl)^{(j)}$ are the elements of the set that includes all of the considered diffracting planes. The final composite pattern is then filtered using high and low pass filters to more accurately reflect variation in the measured EBSD pattern background.

The simulated pattern analysis algorithm begins by measuring a local lattice orientation to within 0.5° using the Hough transform method of standard OIM. A simulated pattern is then generated from the known crystal structure and the Hough transform estimate of the orientation. Cross-correlation analysis as described above is used to compare the ROI shifts from the simulated pattern and the measured EBSD image as illustrated in Fig. 3. The deformation tensor is calculated using geometric relationships and the traction free boundary condition. The fit of the deformation tensor is evaluated by calculating the average error or difference between measured and calculated shifts. Finally, a new pattern is simulated at a deformation state closer to the actual state of the material. This process is repeated iteratively until the deformation converges as close as possible to that of the actual lattice structure.

At present, the resolution of the simulated pattern method does not reach the level of Wilkinson's method. The simulated pattern method can determine the strain and rotation tensors to a resolution of $\pm 7 * 10^{-4}$ indicating a misorientation resolution of ±0.04° [17]. However, though the Wilkinson's method is more accurate, the simulated pattern method readily extends the high resolution advantages to polycrystalline and deformed samples where Wilkinson's method becomes difficult.

Pattern Center Calibration

The pattern center is defined as the intersection of a vector originating from the electron beam/sample interaction point and normal to the plane of the phosphor screen. In order to accurately simulate EBSD patterns for the simulated pattern method, the pattern center must be accurately known to within 1/10th of a pixel [19]. Any error in pattern center calibration propagates into error in the shifts measured by the cross-correlations and results in erroneous measurements of elastic strain and orientation. Indeed, Villert et al. have demonstrated that variation in pattern center parameters leads to artificial measurements and increased error [20]. The cross-correlation function is sensitive to sub pixel shifts in the ROIs. In order to maintain the resolution capabilities of the simulated pattern method, the pattern center must also be calibrated to sub pixel resolution. While standard EBSD analysis software typically calibrates the pattern center with a least squares best fit approach, high resolution cross-correlation methods require higher accuracy calibration.

The necessary accuracy may be obtained by realizing that diffracted electrons create a pattern of bands with parallel edges centered upon great circles of any sphere emanating from the interaction volume (see [21] for an overview of spherical EBSD). The flat phosphor screen distorts these bands such that the band edges no longer appear parallel. But, if the correct pattern center is known, then mapping a collected pattern onto a sphere centered at the interaction volume (as given by the pattern center) must result in a pattern with parallel band edges centered on a great circle. Conversely, if the assumed pattern center is

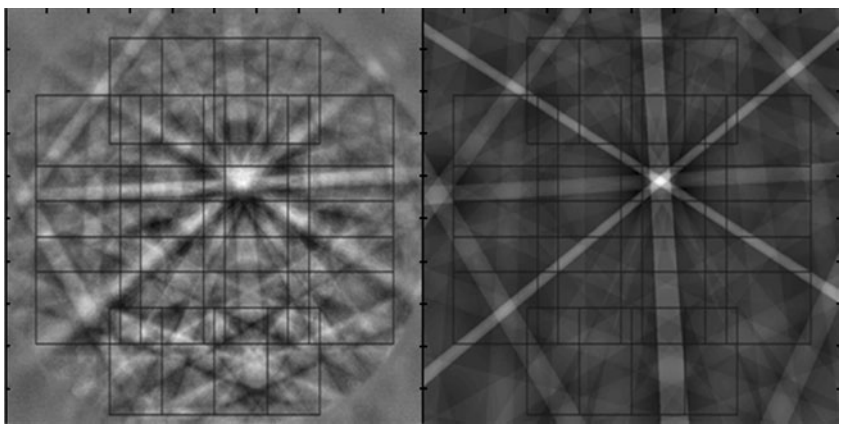

Fig. 3 Measured pattern and a simulated pattern with 20 ROIs outlined for comparison

incorrect, then mapping onto a sphere will not result in parallel band edges centered on great circles.

Several methods for automated pattern center determination are currently in progress and will be described with greater detail in an upcoming specifically dedicated paper. Only a basic overview of one method is included here. Figure 4 shows a collected EBSD pattern which has been mapped onto a sphere using an assumed pattern center location. Simple Bragg's law simulated band edges are overlain on the sphere and artificially widened to ensure capture of the collected bands. For each simulated band that intersects the actual EBSD pattern, the intensity profile is calculated within the simulated band edges by averaging the intensities down the length of the band in small steps moving from one edge to the other. The typical/desired band intensity profile has a central peak with a maximum near the great circle and two troughs equidistant from the center. Various indirect measures of parallelism may be applied to the calculated intensity profiles including: peak intensity maximization, trough intensity minimization, peak to trough difference maximization, trough separation minimization. Such measures have been applied successfully to strain-free single crystal germanium [22, 23].

The right half of Fig. 4 portrays an element of the search space generated by the parallelism approach to pattern center calibration. Optimization may generally be performed discretely through a genetic algorithm, simulated annealing, etc.... It should be noted that only two of the six relevant search space parameters (x*, y*, z*, φ_1, Φ, φ_2) are presented in Fig. 4 and, although the search space appears decidedly smooth at the presented scale, a finer scale reveals a rougher surface. However, at least in the case of single crystal germanium, the noise level of the search space does not prevent a sufficiently accurate pattern center determination.

Measurements: Elastic Strain, Lattice Curvature, and Dislocation Density

At this point a discussion on the relevance and calculation of elastic strain, lattice curvature, and dislocation density is requisite.

For small strains, the elastic strain tensor is simply the symmetric part of the displacement gradient tensor, as given in equation (7a). Knowledge of the elastic strain present in a material is important to possibly resolve the probable failure modes and strain concentration points. The remaining anti-symmetrical portion of the displacement gradient tensor is the material rotation tensor. As discussed by El-Dasher et al., the crystal lattice rotation accounts for a portion of the material rotation [24]. The crystal lattice curvature tensor follows directly from the lattice rotation and as defined by Nye [12] is:

$$k = \begin{bmatrix} k_{11} & k_{12} & k_{13} \\ k_{21} & k_{22} & k_{23} \\ k_{31} & k_{32} & k_{33} \end{bmatrix} \tag{10}$$

where $k_{ij} = \partial\theta_i/\partial x_j$ and the terms θ_1, θ_2, and θ_3 are the lattice rotation about the x_1, x_2, and x_3 coordinates. Clearly, only the first two columns of the curvature tensor can be

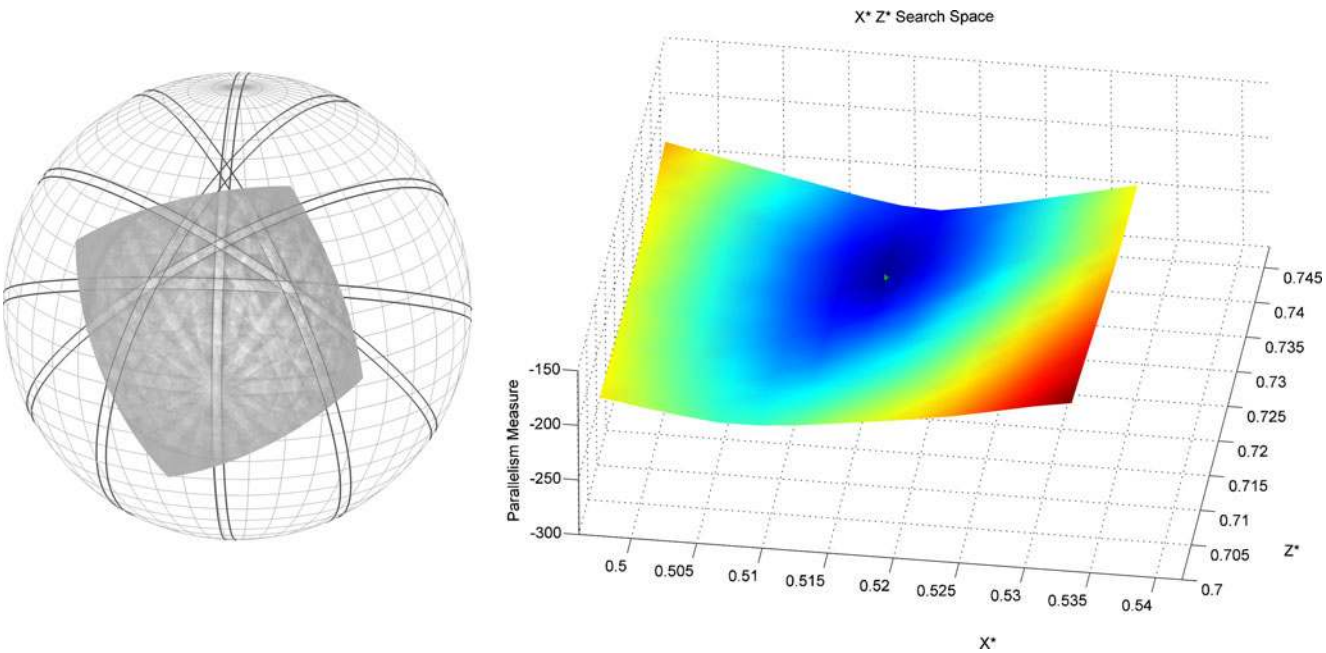

Fig. 4 Parallelism method for pattern center calibration with part of the search space shown on the right. The true pattern center is located at the minimum of the space

obtained from a two-dimensional scan. Access to the third column requires knowledge of local lattice orientation variations perpendicular to the plane of investigation. In the reference state, the lattice curvature is assumed to be zero everywhere, thus the measured curvature is the same as the gradient of lattice rotation.

Nye's dislocation density tensor α_{ij} is related to the lattice curvature tensor as follows (note that the Einstein summation convention is used here and throughout all following discussions):

$$k_{ij} = -\alpha_{ij} + \frac{1}{2}\delta_{ij}\alpha_{kk} - \in_{ijk} \varepsilon^{e}_{jk,l} \tag{11}$$

where δ_{ij} is the Kronecker delta, and $\varepsilon^{e}_{jk,l}$ is the lth derivative of the elastic strain tensor [25]. Therefore, lattice curvature results from the presence of dislocation networks possessing a net Burger's vector, and also from gradients in the elastic strain tensor. Equation (11) implies that the values of three components (α_{i3}) of the dislocation density tensor can be determined with certainty from the 6 accessible curvature components. The other 6 components are obscured by material opacity. If it is determined that the elastic strain gradient terms are negligible, in comparison to the lattice curvatures, than, as Pantleon pointed out, for small misorientations the α_{12}, α_{21}, and the difference between the α_{11} and α_{22} components are also available [26]. It has been the experience of the authors that the elastic strain gradient terms are a factor of ~6 times smaller than the lattice curvature terms [27].

The dislocation density tensor consists of the dislocation densities multiplied by the Burger's vector and associated unit line direction, summed over all dislocation types present [24, 25]. Presented formally:

$$\alpha_{ij} = \sum_{k=1}^{K} \rho^{k} b_{i}^{k} \widehat{z}_{j}^{k} \tag{12}$$

where ρ^k is the density of dislocations of type k, b^k is its Burger's vector, $\widehat{z}^k$ is its unit tangent line direction, and there are K types of dislocations present. Generally the recovery of the full set of ρ^k cannot be completed without ambiguity. The number K of possible dislocation types depends on the geometry of the crystal lattice and the particular dislocation types considered (screw, edge, etc.). Consequently, the number of dislocation types that should be considered usually exceeds the number of components of the dislocation density tensor that are available; and the independent dislocation densities cannot all be determined by inversion of equation (12) [25, 27]. Since at most 5 components of α_{ij} are accessible from two-dimensional scans, the equation is underdetermined and a surfeit of potential solutions exists. Further, there generally are many combinations of Burger's vectors and line directions that support an arbitrary dislocation tensor; therefore, an infinite variety of network types can be envisaged to support the same lattice curvature.

Still, while the exact solutions for dislocation densities are inaccessible, it is possible to solve for a set of densities that satisfies the lattice curvature and minimizes the total required dislocation density. The solution is defined as the geometrically necessary dislocation density and is a lower bound to the solutions of equation (12) (note that the upper bound is infinite) [25, 28]. Knowledge of the lattice curvature and the local geometrically necessary dislocation densities within a material offers information on the stress distribution, provides insight into the deformation mechanics, and indicates likely failure points.

Combining Methods

Wilkinson's method is more accurate than the simulated pattern method and is well suited to measuring gradients. The simulated pattern method is more versatile for polycrystalline scans and measures absolute orientation and strain. Combining the two methods using a custom scan pattern takes advantage of the strengths of each method, providing for accurate measurements of curvature gradients within grains and absolute measurements of elastic strain from grain to grain without requiring multiple strain free reference patterns.

A custom scan pattern like the one in Fig. 5 consisting of closely spaced five-point cross-grids in an evenly spaced hexagonal or square distribution takes full advantage of the two methods. The center points (or other corresponding points) of each cross-grid can be treated separately as a normal scan, and the simulated pattern method can be applied to measure absolute values of elastic strain and rotation. Wilkinson's method is then used to make local estimates of lattice curvature utilizing the five point cross-

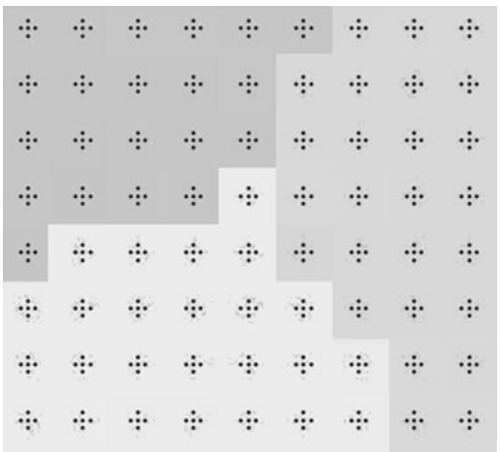

Fig. 5 Schematic of the Cross-Grid method for utilizing both the Simulated Pattern method and Wilkinson's method

grid. Since curvature is a gradient measure, a strain free pattern is not required and the superior accuracy of Wilkinson's method is well applied in finding the curvature and geometrically necessary dislocation density. Obviously, if any two points in the cross are not in the same grain, the calculation is compromised. If temporal limitations are a factor, a five-point grid need not be used. A three-point L-shape provides the same opportunity to use Wilkinson's method for gradient measurements within a grain. However, the five-point grid allows for accuracy-increasing averaging if desired.

Combining the simulated pattern method and Wilkinson's method takes maximum advantage of the available techniques in EBSD analysis to achieve high angular resolution data. Still, neither method increases the spatial resolution of scan data. The following section deals with increasing spatial resolution.

Grain Boundary Spatial Resolution

There exists a finite interaction volume associated with the electron beam. The diameter of the interaction volume depends primarily on the probe current, the sample material, and the accelerating voltage, and is on the order of 100 nm. When the beam scans across a grain boundary, the interaction volume is composed of two or more grains. The resulting EBSD pattern will be a mixture of the patterns from each grain similar to the pattern in Fig. 6, and an additional random noise component associated with the disturbed atomic positions in the interface. Even without any consideration of the random component, the overlapping patterns result in a pronounced decrease in image quality. Additionally, any attempts to analyze an overlapped pattern with either Wilkinson's or the simulated pattern method will likely result in incorrect measurements of strain and rotation as the wrong pattern features are tracked. Correctly separating one grain's contribution to the overlapped EBSD pattern increases spatial resolution and allows for improved accuracy in the study of regions near grain boundaries and triple junctions.

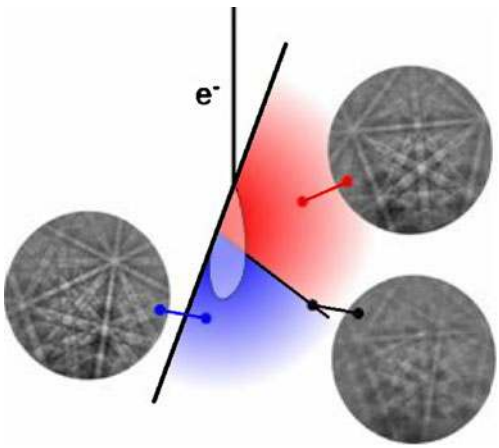

Fig. 6 When the electron beam rasters across a grain boundary portions of the interaction volume will be in separate grains resulting in a mixed pattern that cannot be indexed without adjustment. Figure courtesy of TSL

Kacher et al. proposed the following method for increasing spatial resolution near grain boundaries [29]. To separate a mixed pattern, pristine reference patterns from each of the contributing grains are selected. Each of the reference patterns are then cropped and filtered to secure the highest quality section. A cross-correlation (equation (3)) between the mixed EBSD and the pristine filtered reference patterns shows the fraction of each reference pattern present in the mixed pattern. The zero-shift value of the cross-correlation represents how well the images correspond. The non-dominant reference images are then subtracted out of the mixed pattern leaving only the dominant pattern behind. Finally, the intensity of the remaining image is normalized to correspond with the intensity range found in the unaltered measured patterns. Subsequently, the pattern can be analyzed in the conventional way.

While this method improves the spatial resolution of any scan crossing a grain boundary, it does not necessarily locate the grain boundary exactly at the surface if the investigated boundary is heavily inclined. Because the electron interaction volume extends 10–40 nm below the surface, the point where the dominant pattern switches occurs when equal amounts of electrons are returning from each grain [30]. Depending upon the inclination of the boundary, this point could be arbitrarily shifted. However, regardless of the boundary inclination, the pattern separation method improves measurement accuracy with the highest spatial resolution obtained being an average of half the interaction volume at the grain boundary. Separating patterns allows orientation measurements to be taken right up to the very edge of the grain boundary. While other phenomena, such as dislocation pileups at grain boundaries, can cause a decrease in image quality and consequently limit spatial resolution, if a discernable pattern is acquired (mixed or not) accurate measurements can be taken. Figure 7 shows the results of a simulation demonstrating the accuracy attainable by pattern separation. The labelled ESBD patterns 1–5 represent a series of artificially mixed images with intensity filtering and image quality adjustments to represent actual patterns near a grain boundary (without a random component). Pattern 1 is unmixed (but contains elastic strain), pattern 2 contains 75% of pattern 1 and 25% of pattern 5 (also containing elastic strain), pattern

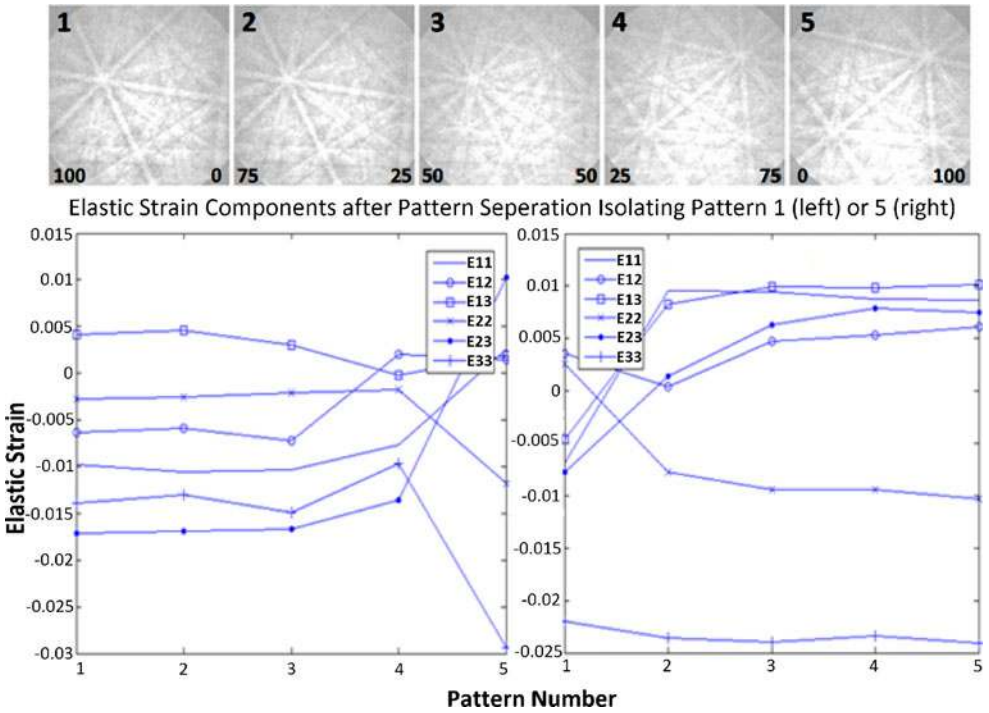

Fig. 7 Effect of pattern separation at various levels of pattern mixing on components of the elastic strain tensor

3 is split evenly between 1 and 5, etc.... Each mixed patterns was separated and measurements were made using the simulated pattern method. Ideally, the elastic strains represented in the figure would not vary across the patterns, but as expected, the smaller the percentage of an unmixed pattern contained in a mixed one, the greater the measurement error. Still, at 25 and 50% mixing, a majority of the separated measurements compare favourably with the unmixed values.

Experiments

For this work, the above techniques were applied to three samples, each of which will be presented here as examples of the information obtained by advanced EBSD analysis. The first example deals primarily with calculation of the elastic strain tensor, the rotation tensor, lattice curvature, and geometrically necessary dislocation density. The second example is more concerned with advantages of the combined L-grid scanning method. And the third scan deals specifically with pattern separation at grain boundaries.

Single Crystal Nickel Indentation

The first experiment is a wedge indentation which is subjected on a single crystal nickel sample. The geometry of the problem is designed such that only three effective in-plane slip systems exist. Rice showed that plane deformation conditions are satisfied when a face centered cubic crystal is subjected to a line loading parallel to a [110] direction. The experiments and sample preparation for EBSD were done on a Nickel single crystal sample by J. W. Kysar's group at Columbia University. The EBSD scans were done at BYU. Two scans of the indented sample were examined: the first is a 100 μm square scan with a 500 nm step size, and the second is a smaller 10 μm by 5 μm scan with a 50 nm step size. Maps of the resultant elastic strain tensor are given in Fig. 8. Note that the wedge penetrates the sample from the bottom center position of these figures. The first maps give the diagonal components of the strain tensor and the second three the off diagonal. It can be seen that the indentation and ensuing structural changes result in regions of residual elastic compression and tension in a wide ranging area extending beyond the borders of even the larger scan. Additionally, the most strongly affected regions appear to have a structure of contrasting elastic strain, from left to right in each example. It is instructional to note the regional interdependence of the various strain components.

In addition to the elastic strain tensor, the lattice rotation was determined by comparing the as-deformed orientation of the crystal lattice to its known orientation in the undeformed reference state as discussed in [31]. Figure 9 shows the θ_z component of the rotation tensor in degrees. The larger scan shows how the lattice tends to curve out

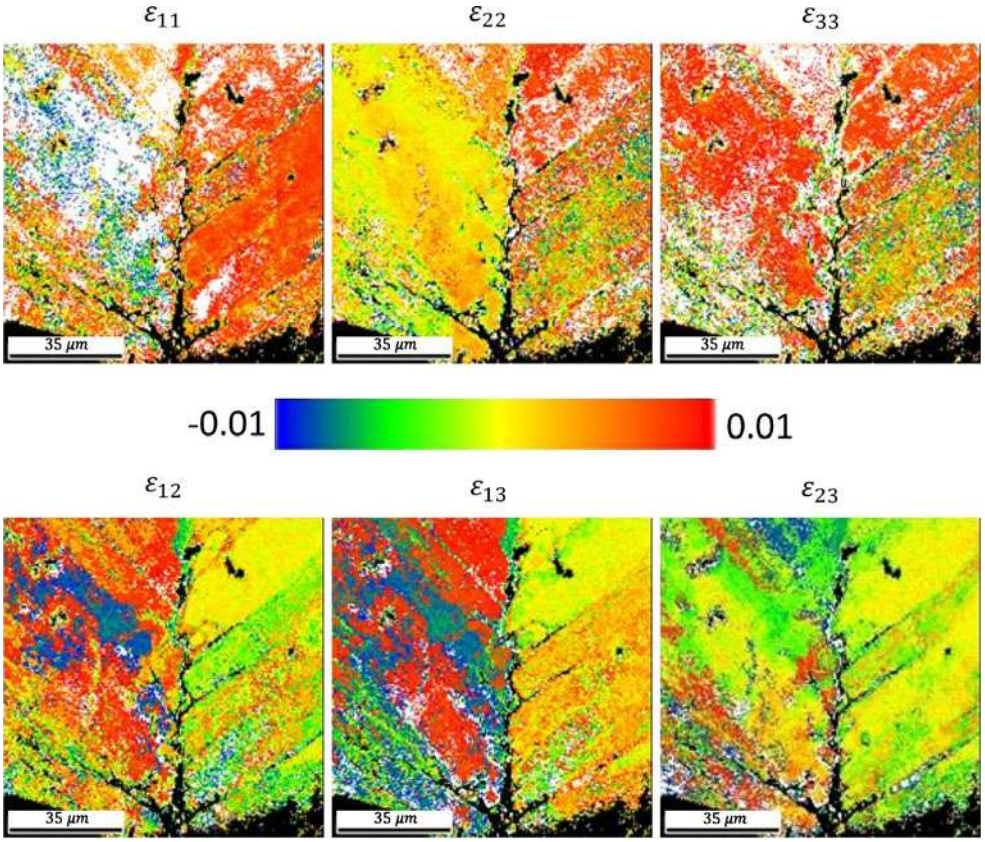

Fig. 8 Mapped components of the elastic strain tensor ranging from −0.01 to 0.01

away from the centrally affected region and how stark the difference is on either side. This region of rapid change in lattice rotation was identified in a previous study using a spatial resolution of 3 microns [32]. The higher spatial resolution analysis herein showed that the change in lattice rotation is not discontinuous, but the lattice curvature is very high. Knowledge of the rotation tensor, leads easily to calculations of the lattice curvature as defined by equation (10). While it is possible to display the components individually, the sum of the magnitudes of the six available curvature components is mapped in Fig. 10. The summed curvature increases sharply near the highly deformed central areas and could signal a probable propagation path of material failure in components where similar features might occur.

Finally, from knowledge of lattice curvature it is possible to calculate a lower bound of geometrically necessary dislocations. Kysar et al. derived the least L^2-norm

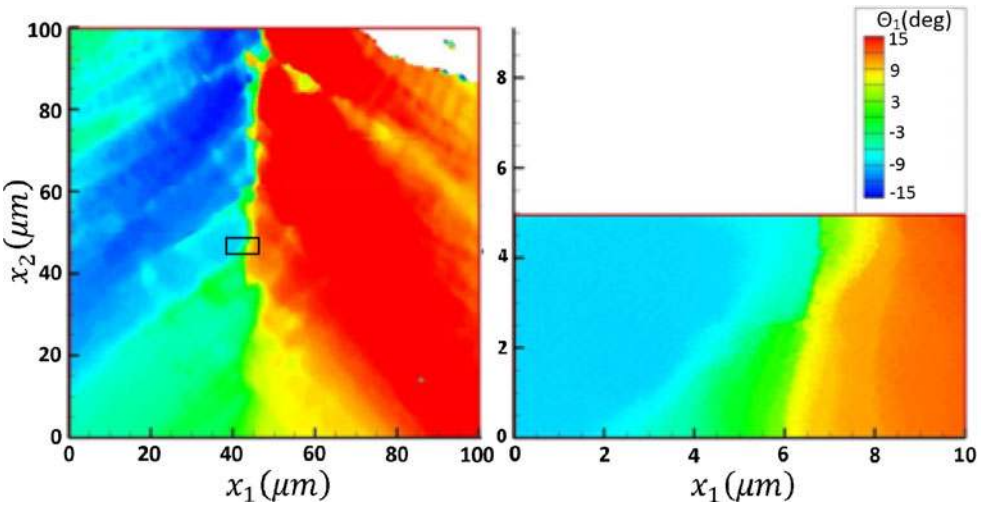

Fig. 9 θ_z component of the rotation tensor mapped across a 100 μm square area and a 5 μm by 10 μm area respectively

solutions to the geometrically necessary dislocation densities for the special cases where there are three effective in-plane slip systems [33]. Figure 11 shows that the density of GND's is much higher through the central area. The high gradient in lattice rotations in this region results in accumulation of dislocation densities. Further, there appears to be a characteristic length scale to the concentrated region of GND's on the order of ~1 μm. In this particular sample, the width of the densest regions is consistent, whether near or far from the indentation point.

Cold-worked Polycrystalline Copper Sample

In addition to the single crystal indentation experiment, a second experiment was performed on a polycrystalline 58 percent cold-worked copper sample. The sample was polished and scanned utilizing an L-grid scanning pattern to obtain increased measurement accuracy in a reasonable scan time. The scan area is 100 μm square, with a 1 μm step size between L-grid center points and 100 nm spacing between points within each grid. Thus, identical measurement resolution in a square scan of similar size would have required one million individual scan points. However, using the L-grid technique, only 30 thousand points were required; a remarkable 97 percent increase in efficiency with minimal loss of usable information. Wilkinson's method was used to determine the lattice orientation gradient within grains and the simulated pattern adaptation was used to obtain absolute measurements of strain and rotation across the polycrystalline sample. The resultant false color grain map is shown in Fig. 12.

The elastic strains over the entire sample were obtained using the simulated pattern method. Some components are presented in Fig. 13. It is interesting to note the rather uniform strain distribution across each particular grain interior while wide variations exist near boundaries. Additionally, the lattice curvature was calculated using Wilkinson's method using the L-grid. Figure 14 shows the mapped sum of the absolute magnitudes of the six obtainable components of the curvature tensor. Wide variations in the curvature occur near grain boundaries as expected. Additionally, the interior concentrations of curvature variation are likely due to a distributed pattern of internal dislocation cell structures resulting from the material rolling.

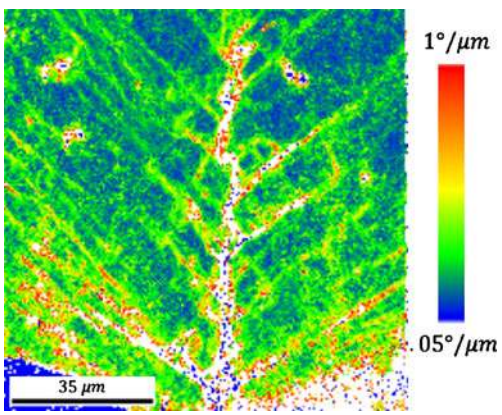

Fig. 10 Summed available components of the curvature

Rolled Polycrystaline Nickel Sample

Finally, the pattern separation method was employed on a set of consecutive points (across a grain boundary) from a polycrystalline nickel line scan to illustrate the increased measurement accuracy available. As described in the final portion of the Materials and Methods segment, the cross-correlation of mixed patterns at the grain boundary with ideal reference patterns from each respective grain was performed. Upon comparison of the intensity peaks, a decision was made and the secondary part of the mixed pattern was subtracted out. One of the mixed patterns and two reference patterns are shown in Fig. 15. In this particular case, cross-correlation revealed that the grain on the right was the main contributor to the mixed diffraction pattern and therefore the left reference pattern was subtracted.

Mixed patterns result in errors and inaccuracies for the recovered strain and the rotation tensors, which increase as the beam approaches the interface. Without pattern separation, the measured values of strain and rotation may be artificially low or high. While it goes beyond the purposes of this paper to delve into the changes upon each component of the strain and rotation tensors at one particular grain boundary, suffice it to say that pattern separation has a significant effect on the measurements at and near grain boundary interfaces. Figure 16 provides one example: pattern separation reveals that the un-separated measurement of ε_{22} is artificially low, particularly just before and after crossing the grain boundary. Further, the location of the grain boundary is ~1 μm further along the progression. The change in grain boundary position is large when compared to the estimated ~100 nm spatial resolution, however, the discrepancy disappears upon recollection of the 1 μm step size used for this particular scan. Essentially, the pattern separation method demonstrated that a single mixed pattern very near the OIM grain boundary produced a faulty result for the ε_{22} elastic strain that subsequently misplaced the approximated grain boundary by one micron (note that this particular boundary is probably at a high angle of inclination from the surface, accounting for the wide range of partially mixed patterns and subsequent positional change). To obtain the upper limits of spatial resolution, a sufficiently small step size must be used in correlation with the pattern separation

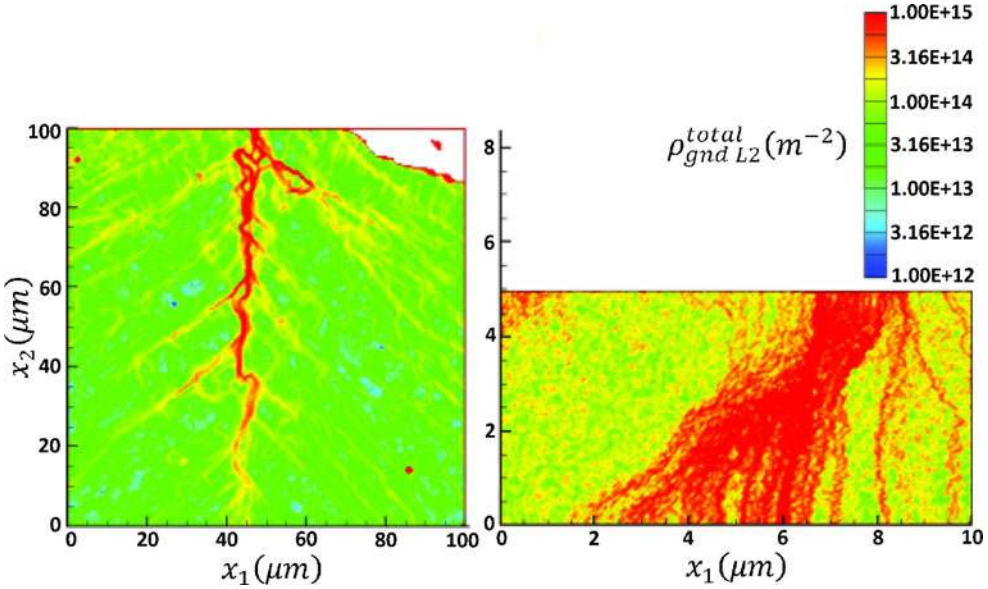

Fig. 11 GND density for large and small scans demonstrating concentrations near failure points

method. The increased spatial resolution available from pattern separation could play a vital role in furthering the study of grain boundary interactions with the deformation field, by making near interface measurements possible. Figure 16 is representative of the useful increases in accuracy pattern separation affords.

Discussion

Increased informational content can be extracted from EBSD analysis through the appropriate application of various advanced methodologies. To summarize: Wilkinson's method is ideal for measuring gradient terms and for application in single crystal samples with readily available strain-free reference patterns. The simulated pattern method cannot yet equal Wilkinson's method in terms of angular resolution, but extends the measurement capabilities into polycrystalline and highly deformed samples. Pattern center calibration is vital to insure accuracy in measurements of elastic strain, lattice curvature, and dislocation density. Combining the two cross-correlation methods can take advantage of the strengths of each. And finally, spatial resolution can be improved by cross-correlations that are used to separate out non-dominant patterns near interfaces. It should be noted that the usefulness of each of these techniques is restricted to materials which allow a fine polish and produce an EBSD pattern. Materials which are porous, amorphous, not polishable, etc., will require different methods.

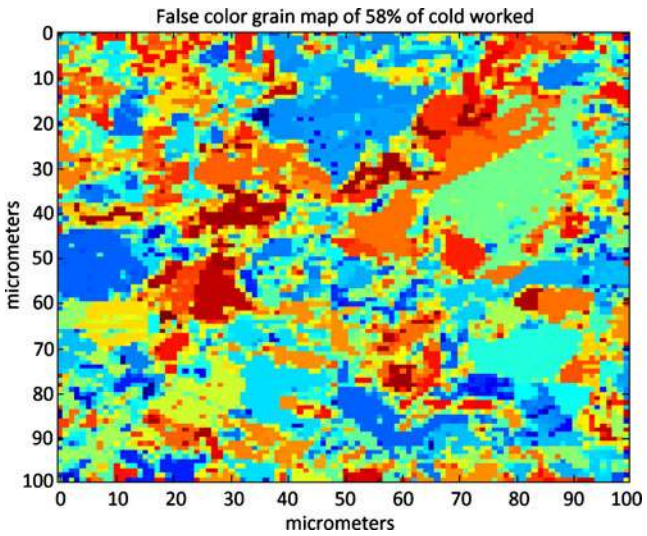

Fig. 12 False color grain map of cold-worked copper

Each of the above techniques has been successfully applied to an indented single crystal sample, a polycrystalline sample, or both. The advantages of increased resolution, both spatial and angular, are obvious in light of the stunning images obtained, which contain a wealth of information that can shed light on the pertinent micromechanics. The potential for greater understanding of crack initiation is particularly promising. Further study is necessary to determine the potential resolution of crack detection, but it seems reasonable to postulate that even micro cracks within an order of magnitude of the interaction volume diameter may be detectable. Still, limitations in instrument capability and the lack of three-dimensional information leaves ample room for future improvement and innovation. At present, measurements of elastic strain, rotation, lattice curvature, and dislocation density are limited to the material surface and the effect of the traction free condition on each

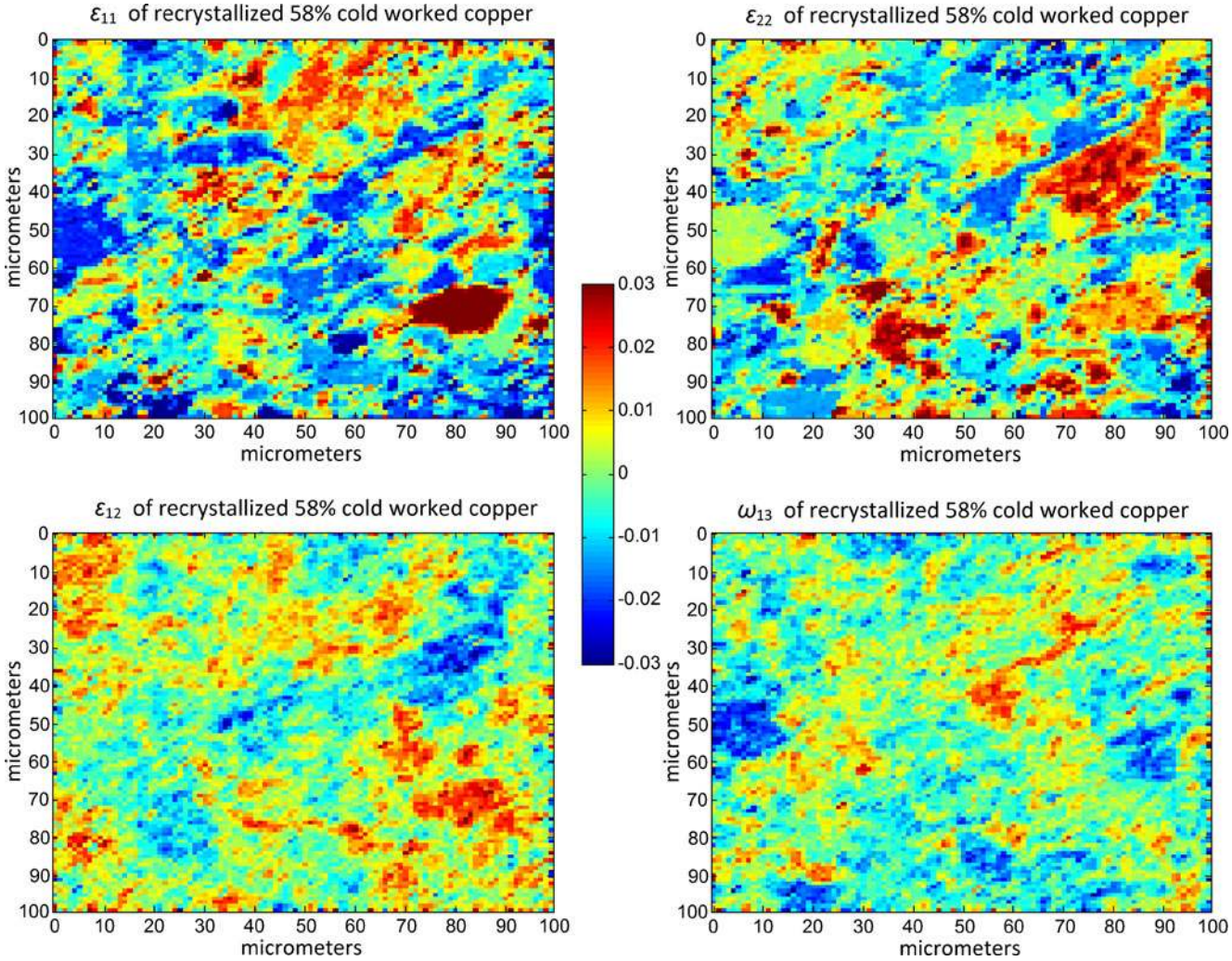

Fig. 13 Mapped components of the elastic strain tensor of cold-worked copper

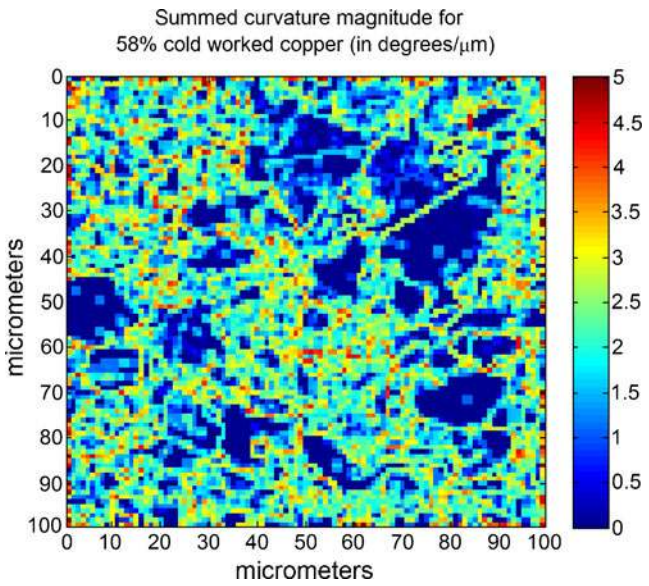

Fig. 14 Summed lattice curvature of cold-worked copper

metric must be considered. In the study of crack initiation (which typically occurs at the surface) this observational restriction is probably not an issue, but sectioning a sample to investigate the interior structure introduces a free surface which may substantially alter any recovered measurements. Regardless, the lattice configuration within ~100 nm of the surface may be reliably investigated using the advanced techniques herein presented.

Conclusions

To conclude, the current state of EBSD-based microstructure analysis has been outlined and examples of the various methods provided. The current absolute resolution limits are given by Wilkinson's method at 0.006° for angular and 10^{-4} for strain components. The simulated pattern augmentation offers resolutions of 0.04° and 7×10^{-4}, respectively, while allowing greater versatility in measurements for

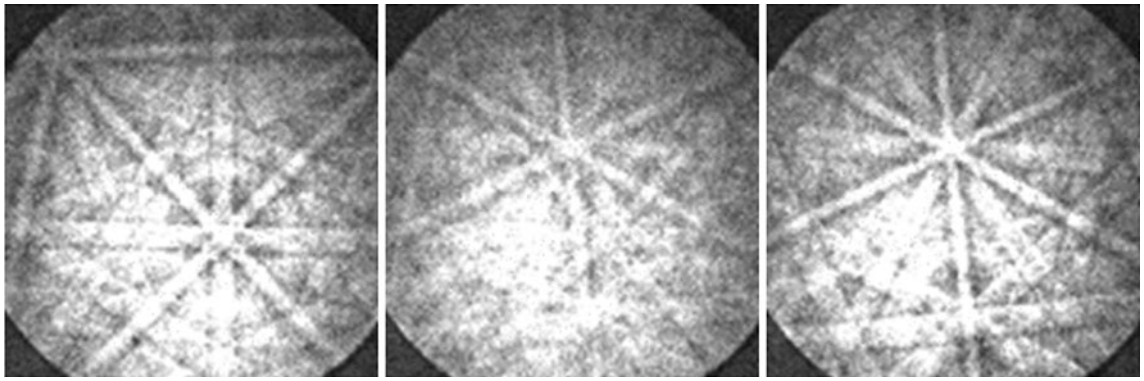

Fig. 15 A mixed grain boundary pattern in the center and two reference patterns from the mixed grains on either side of a rolled nickel line scan

polycrystals. Pattern center calibration, accomplished by parallelizing band edges in a spherical frame, can reduce pattern center error to a negligible level (i.e. below the noise level of Wilkinson's method). Only 6 components of the lattice curvature tensor are available from a two-dimensional scan and at most 5 components of Nye's dislocation density tensor can be resolved. Individual dislocation densities generally cannot be recovered, but a lower bound density can be established. Finally, separating mixed boundary patterns using cross-correlation facilitates accurate measurements nearer to interfaces than otherwise would be possible.

Acknowledgements The authors wish to acknowledge funding from the Army Research Office, Dr. David Stepp Program Director. JWK acknowledges support from the National Science Foundation (NSF-0706058), Air Force Office of Scientific Research (AFOSR FA9550-09-1-0048), and Lawrence Livermore National Laboratory (LLNL-B585562).

References

1. Bieler T, Eisenlohr F, Roters F, Kumar D, Mason D, Crimp D, Raabe D (2009) The role of heterogeneous deformation on damage nucleation at grain boundaries in single phase metals. Int J Plast 25(9):1655–1683
2. Przybyla CP, McDowell DL (2010) Microstructure-sensitive extreme value probabilities for high cycle fatigue of ni-base superalloy in100. Int J Plast 26(3):372–394
3. Adams BL, Wright SI, Kunze K (1993) Orientation imaging: the emergence of a new microscopy. Metall Mater Trans A 24 (4):819–831
4. Wright SI (1993) A review of automated orientation imaging microscopy(oim). J Comput-Assist Microsc 5(3):207–221
5. Humphreys FJ, Huang Y, Brough I, Harris C (1999) Electron backscatter diffraction of grain and subgrain structures—resolution considerations. J Microsc 195(3):212–216
6. Ren SX, Kenik EA, Alexander KB, Goyal A (1998) Exploring spatial resolution in electron back-scattered diffraction experiments via monte carlo simulation. Microsc Microanal 4(1):15–22
7. Tao X, Eades A (2004) Monte carlo simulation for electron backscattering diffraction. Microsc Microanal 10(2):940–941
8. Bate PS, Knutsen RD, Brough I, Humphreys FJ (2005) The characterization of low-angle boundaries by EBSD. J Microsc 220 (1):36–46
9. Zaefferer S (2007) On the formation mechanisms, spatial resolution and intensity of backscatter kikuchi patterns. Ultramicroscopy 107(2–3):254–266
10. Troost KZ, van der Sluis P, Gravesteijn DJ (1993) Microscale elastic-strain determination by backscatter kikuchi diffraction in the scanning electron microscope. Appl Phys Lett 62(10):1110
11. Wilkinson AJ, Meaden G, Dingley DJ (2006) High resolution mapping of strains and rotations using electron backscatter diffraction. Mater Sci Technol 22(11):1271–1278
12. Nye JF (1953) Some geometrical relations in dislocated crystals. Acta Metall 1:153–162
13. Lewis JP (1995) Fast template matching. Proc Canad Imag Proc 95:120–123
14. Tao X, Eades A (2005) Errors, artifacts, and improvements in EBSD processing and mapping. Microsc Microanal 11(1):79–87
15. Tao X, Eades A (2005) Measurement and mapping of small changes of crystal orientation by electron backscattering diffraction. Microsc Microanal 11(4):341–353
16. Wilkinson AJ, Meaden G, Dingley DJ (2006) High-resolution elastic strain measurement from electron backscatter diffraction patterns: new levels of sensitivity. Ultramicroscopy 106(4–5):307–313
17. Kacher J, Landon CD, Adams BL, Fullwood DT (2009) Bragg's law diffraction simulations for electron backscatter diffraction analysis. Ultramicroscopy 109(9):1148–1156
18. Winkelmann A (2008) Dymical effects of anisotropic inelastic scattering in electron backscatter diffraction. Ultramicroscopy 108 (12):1546–1550

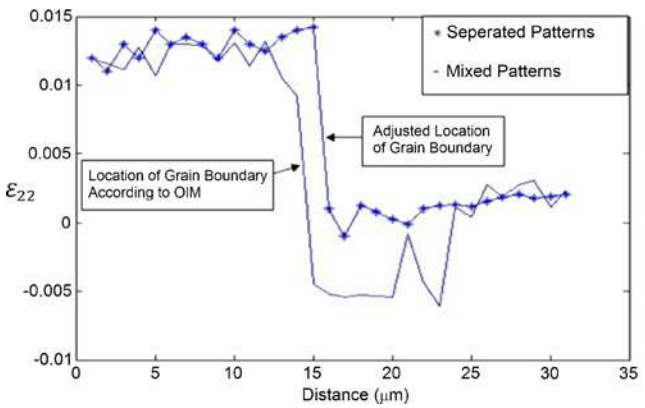

Fig. 16 Effect of pattern separation on strain measurements at a grain boundary

19. Gardner CJ, Adams B, Basinger J, Fullwood DT (2010) EBSD-based continuum dislocation microscopy. Int J Plast 26:1234–1247
20. Villert S, Maurice C, Wyon C, Fortunier R (2009) Accuracy assessment of elastic strain measurement by EBSD. J Microsc 233 (2):290–301
21. Day AP (2008) Spherical EBSD. J Microsc 230(3):472–486
22. Kacher J, Basinger J, Adams BL, Fullwood DT (2010) Reply to comment by maurice et al. In response to "Bragg's law diffraction simulations for electron backscatter diffraction analysis." Ultramicroscopy 110(7):760–762
23. Basinger J, Fullwood DT, Kacher J, Adams B (2010) Precision pattern center approximation in EBSD by the method of parallelism. Microsc Microanal (In Review)
24. Sun S, Adams BL, King WE (2000) Observations of lattice curvature near the interface of a deformed aluminium bicrystal. Philos Mag, A, Phys Condens, Matter, Struct Defects Mech Prop 80(1):9–25
25. Kröner E (1958) Kontinuumstheorie der versetzungen und eigenspannungen, vol 5. Springer, Berlin
26. Pantleon W (2008) Resolving the geometrically necessary dislocation content by conventional electron backscattering diffraction. Scr Mater 58:994–997
27. Landon CD, Adams B, Kacher J (2008) High resolution methods for characterizing mesoscale dislocation structures. J Eng Mater Technol 130(2):021004–021008
28. El-Dasher BS, Adams BL, Rollett AD (2003) Viewpoint: experimental recovery of geometrically necessary dislocation density in polycrystals. Scr Mater 48(2):141
29. Kacher J, Adams BL, Fullwood D, Landon C (2008) Seperating coincident electron backscatter diffraction patterns near interfaces. Ceram Trans 201:147–154
30. Dingley DJ (2004) Progressive steps in the development of electron backscatter diffraction and orientation imaging microscopy. J Microsc 213(3):214–224
31. Kysar JW, Saito Y, Oztop MS, Lee D, Huh WT (2010) Experimental lower bounds on geometrically necessary dislocation density. Int J Plast 26:1097–1123
32. Rice JR (1987) Tensile crack tip fields in elastic-ideally plastic crystals. Mech Mater 6:317–335
33. Kysar JW, Gan YX, Morse TL, Chen X, Jones ME (2007) High strain gradient plasticity associated with wedge indentation into face-centered cubic single crystals: Geometrically necessary dislocation densities. J Mech Phys Solids 55(7):1554–1573